JOURNAL OF THERMOPHYSICS AND HEAT TRANSFER
Vol. 22, No. 1, January–March 2008

One-Dimensional Ablation Using a Full Newton's Method and Finite Control Volume Procedure

A. J. Amar*
Sandia National Laboratories,
Albuquerque, New Mexico 87185-0825 and North Carolina State University,
Raleigh, North Carolina 27695-7910
B. F. Blackwell†
Blackwell Consulting, Corrales, New Mexico 87048
and
J. R. Edwards‡
North Carolina State University, Raleigh, North Carolina 27695-7910

DOI: 10.2514/1.29610

The development and verification of a one-dimensional constant density material thermal response code with ablation is presented. The implicit time integrator, control volume finite element spatial discretization, and Newton's method (with an analytical Jacobian) for the entire system of residual equations have been implemented and verified for variable material properties, Q^* ablation, and thermochemical ablation problems. Timing studies were performed, and when accuracy is considered, the method developed in this study exhibits significant time savings over the property lagging approach. In addition, maximizing the Newton solver's convergence rate by including sensitivities to the surface recession rate reduces the overall computational time when compared to excluding recession rate sensitivities.

Nomenclature

A	=	area, m^2
$\boldsymbol{A}$	=	area vector, m^2
B'_c	=	nondimensionalized char ablation rate
C_h	=	corrected heat transfer Stanton number
C_{h_o}	=	uncorrected heat transfer Stanton number
C_m	=	mass transfer Stanton number
C_p	=	specific heat at constant pressure, $J/kg \cdot K$
C_v	=	specific heat at constant volume, $J/kg \cdot K$
$\dot{E}$	=	element energy convection rate, W
E	=	energy content, J
e	=	specific internal energy, J/kg
(e)	=	element
h	=	specific enthalpy, J/kg
k	=	thermal conductivity, $W/m \cdot K$
L	=	time-dependent domain length, m
$\dot{m}''$	=	mass loss rate per unit area, $kg/m^2 \cdot s$
N	=	shape function
Pr	=	Prandtl number
$\dot{Q}$	=	element heat conduction rate, W
Q^*	=	heat of ablation, J/kg
$\dot{q}''$	=	heat flux, W/m^2
$\boldsymbol{\dot{q}}''$	=	heat flux vector, W/m^2
R	=	residual
r	=	recovery factor
s	=	surface recession, m
$\dot{s}$	=	surface recession rate, m/s
T	=	temperature, K
t	=	time, s
u	=	control volume boundary velocity, m/s
$\boldsymbol{u}$	=	velocity vector, m/s
V	=	volume, m^3
x	=	coordinate with respect to instantaneous ablation front, m
z	=	coordinate with respect to initial ablation front, m
$\dot{z}$	=	nodal velocity, m/s
α	=	thermal diffusivity, m^2/s
δ	=	temperature perturbation, K
ϵ	=	emissivity
η	=	Landau coordinate
θ	=	transformed temperature, K
λ	=	blowing reduction parameter
ξ	=	local coordinate
ρ	=	density, kg/m^3
σ	=	Stefan–Boltzmann constant, $W/m^2 \cdot K^4$
Ω	=	Stanton number correction

Subscripts

abl	=	ablation
ah	=	aerodynamic heating
back	=	back boundary
blw	=	blowing
cw	=	cold wall
e	=	boundary layer edge condition
full	=	full sensitivity matrix
hw	=	hot wall
iter	=	iterative solution procedure
j	=	nodal index
lag	=	property lagging solution procedure
o	=	initial value
r	=	recovery value
rad	=	radiation

Presented as Paper 2910 at the 9th AIAA/ASME Joint Thermophysics and Heat Transfer Conference, San Francisco, California, 5–8 June 2006; received 5 January 2007; revision received 21 March 2007; accepted for publication 27 March 2007.

*Graduate Student Intern, Aerosciences and Compressible Fluid Mechanics Department; currently at NASA Johnson Space Center, Applied Aeroscience and CFD Branch. Member AIAA.

†Sandia National Laboratories Consultant; Adjunct Professor, North Carolina State University, Department of Mechanical and Aerospace Engineering. Associate Fellow AIAA.

‡Associate Professor, Department of Mechanical and Aerospace Engineering. Associate Fellow AIAA.

ref = reference value
res = reservoir property
s = solid property
tri = tridiagonal sensitivity matrix
w = property of gases adjacent to the wall

Superscripts

n = time level
v = iteration level
$*$ = reference value

I. Introduction

FOR nearly half a century, numerical heat transfer and ablation modeling have been important tools in the design and analysis of rocket nozzles and reentry vehicle heat shields because they provide a means of simulating material thermal response including transient heat conduction, shape change, and in-depth decomposition. Accurate prediction of mass loss and energy transfer helps minimize vehicle weight while still maintaining the nozzle lining's or heat shield's protective capabilities. In the 1960s, Moyer and Rindal [1] developed a one-dimensional, finite difference ablation code (Charring Materials Ablation, CMA) that employed a translating grid scheme in which the grid was attached to the receding surface, and the overall number of nodes in the domain would be reduced as mass was removed at the ablating surface. With this method, each node translates with the same velocity as the surface, and the size of grid cells remains fixed except for the back boundary cell which reduces in size until the cell has reached a critical thickness. This "node-dropping" translating grid scheme was a common approach during the 1960s and 1970s and is still used today.

Moyer and Rindal used a fully implicit time integrator and lagged the temperature-dependent material properties and surface recession rate at the interior nodes while the nonlinear surface energy balance was solved iteratively to give the updated surface recession rate. Explicit integration of the energy equation has also been attempted by Moyer and Rindal during the development of CMA and more recently in a finite volume code by Suzuki et al. [2]. In 1988, Blackwell [3] presented the control volume finite element method (CVFEM) for solving ablation problems on translating/node-dropping grids with a fully implicit time integrator with which he implemented the Moyer and Rindal approach to iterating only on the nonlinear surface energy balance.

Later, a contracting grid scheme for one-dimensional ablation was presented by Blackwell and Hogan [4] in which the relative size of the grid cells and the total number of cells remain fixed throughout the problem, and each node translates at a fraction of the surface recession rate. This eliminates the node-dropping complexity, but adds a change in energy storage due to cell volume reduction. This method also has a more logical extension to multiple dimensions as presented by Hogan et al. [5]. Blackwell's and Hogan's work also implemented the CVFEM with a fully implicit time integrator that again iterated only on the surface energy balance to determine recession rate. More recent studies on one-dimensional and multidimensional ablation modeling and application work can be attributed to Suzuki et al. [6] and Chen and Milos [7–9].

The current study is a presentation of the development and verification of a one-dimensional thermal response and ablation code using the CVFEM, a contracting grid scheme, and fully implicit time integration. In addition, Newton's method in residual form is used to iterate on the entire system of equations to determine the time accurate temperature-dependent properties and surface recession rate. For a full implementation of Newton's method, the residual equations' sensitivities to surface recession rate must be included, which causes the linearized system to deviate from its traditional tridiagonal structure. Finite difference sensitivities could be used for the Jacobian terms, but an analytic approach is presented here. Although iterating on the entire system of equations is more expensive on a per time level basis, results are presented that show the increase in accuracy allows for larger time steps and an overall reduction in computational time to achieve the same accuracy compared to a property lagging approach.

Although the model has been developed with in-depth decomposition and gas phase continuity for planar, cylindrical, and spherical geometries, only the solution of the energy equation for a nondecomposing material including conduction, capacitance, and grid convection terms for planar geometries is presented. The simplifications presented in this paper are present so that the development, verification, and usability of the approach can be more clearly presented. Modern software development should include both formal verification and validation studies to ensure that the model equations have been implemented correctly and that they properly account for the physics of the problem being solved. It is the intent of the authors to show the algorithm development and systematic verification process that was adopted throughout this code development project because verification results for similar codes are sparse. As a result, the physical model presented in this work does not apply to any specific ablation problem that an analyst or researcher may be faced with, but the software development approach and novel solution procedure for this class of problems can be extended to include more complicated and applicable physics. The results presented in this paper are a necessary step in the process of developing an ablation code with more complex physical models. Amar [10] presents the extension of the model detailed in this paper to include in-depth decomposition and pyrolysis gas flow through the char layer, and ongoing efforts exist to improve the implementation of the surface chemistry model.

II. Governing Equations

The energy equation for an arbitrary control volume is given by

$$\iint_A \dot{\boldsymbol{q}}'' \cdot \mathrm{d}\boldsymbol{A} - \iint_A \rho h \boldsymbol{u} \cdot \mathrm{d}\boldsymbol{A} + \frac{\mathrm{d}}{\mathrm{d}t} \iiint_V \rho e \, \mathrm{d}V = 0 \tag{1}$$

where the first integral represents the net heat conducted out of the control volume, the second integral is the net enthalpy flux out of the control volume resulting from control volume boundary translation, and the third integral is the time rate of change of energy stored in the control volume resulting from the internal energy of the material. For the current study, it will be assumed that the material does not decompose internally; therefore, reactions only occur at the ablating surface and the material has a uniform density. For one dimension, Eq. (1) in semidiscrete form becomes

$$(\dot{q}''A)_{j+1/2} - (\dot{q}''A)_{j-1/2} + (\rho A u h)_{j-1/2} - (\rho A u h)_{j+1/2} + \frac{\mathrm{d}}{\mathrm{d}t} \int_{z_{j-1/2}}^{z_j} \rho e \, \mathrm{d}V + \frac{\mathrm{d}}{\mathrm{d}t} \int_{z_j}^{z_{j+1/2}} \rho e \, \mathrm{d}V = 0 \tag{2}$$

where the control volume boundaries are denoted by the $1/2$ indices and are located at element midpoints as seen in Fig. 1.

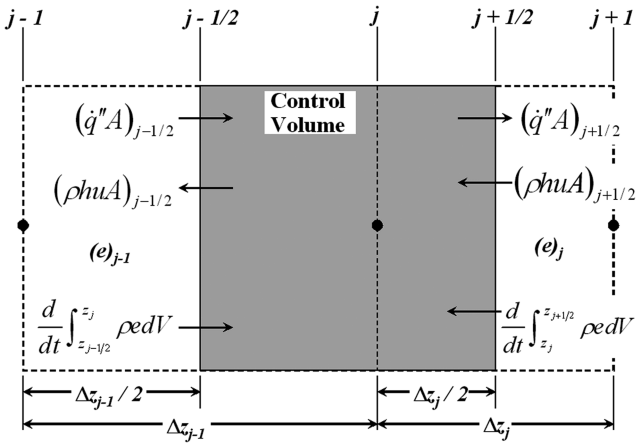

Fig. 1 Schematic of control volume surrounding node j with elements $(e)_{j-1}$ and $(e)_j$.

III. Contracting Grid Scheme

The mesh movement scheme implements the Landau [11] coordinate system as presented by Blackwell and Hogan [4]. It redefines the spatial coordinate such that the nondimensional thickness of the remaining domain in Landau space is always unity and that the Landau coordinate of a given node is constant throughout the problem. As seen in Fig. 2, the z-coordinate system is fixed with its origin at the initial ablation front while the x coordinate is attached to the instantaneous ablation front. The Landau coordinate at any location is given as

$$\eta = \frac{L - x}{L} = \frac{L_o - z}{L_o - s} \tag{3}$$

It is evident that at the ablation front, $x = 0$, $z = s$, and $\eta = 1$, while at the back face, $x = L$, $z = L_o$, and $\eta = 0$. As a result, the translation of any node in a given time step is

$$z_j^{n+1} - z_j^n = \eta_j \dot{s}^{n+1} \Delta t^{n+1} \tag{4}$$

Consequently, the velocity of any node can be related to the surface recession rate by

$$\dot{z}_j^{n+1} = \eta_j \dot{s}^{n+1} \tag{5}$$

Because control volume boundaries are at element centers, the velocity of the control volume boundary is given by

$$u_{j+1/2}^{n+1} = \dot{s}^{n+1} \tfrac{1}{2}(\eta_j + \eta_{j+1}) \tag{6}$$

Figure 3 shows an initial to final mesh comparison for a one-dimensional uniform mesh problem for both translating and contracting grid schemes. Although the nodal displacement relationship is simpler for the translating grid scheme, it creates a large discontinuity in adjacent cell sizes at the back face which could have negative numerical implications on the spatial discretization accuracy. Also, the contracting grid scheme avoids the node-dropping complexity and ensures that the spatial accuracy of the scheme is maintained throughout the problem because the number of nodes and the dimensionless element thickness $[\Delta z_j(t)/L(t)]$ is constant.

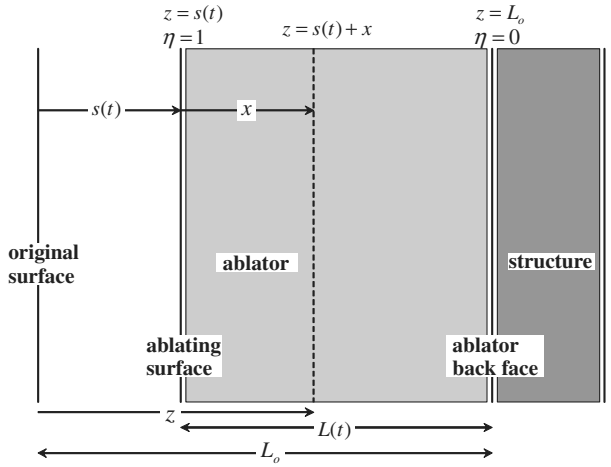

Fig. 2 Schematic of coordinate systems for one-dimensional planar geometry.

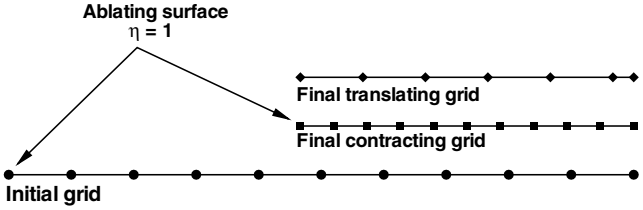

Fig. 3 Initial-to-final mesh comparison for contracting grid scheme on a uniform mesh.

IV. Element Sensitivity Matrices

Element sensitivity matrices were derived for the conduction, convection, and capacitance terms in the energy equation where nodal temperatures and surface recession rate were treated as the independent variables.

A. Conduction

Fourier's law is used to model the heat conducted at a control volume boundary which is given by

$$\dot{Q}_{j+1/2} = \left[-k(T)A\frac{\partial T}{\partial z}\right]_{j+1/2} = \frac{-\bar{k}(T)A}{\Delta z_j}(T_{j+1} - T_j) \tag{7}$$

where $\Delta z_j = z_{j+1} - z_j$, $\bar{P} = (P_{j+1} + P_j)/2$, and P is any quantity. A sign convention will be adopted such that an energy flux out of a control volume is a positive quantity. Thus, the element representation of the heat conduction rate is given by

$$\begin{bmatrix} \dot{Q}_j \\ \dot{Q}_{j+1} \end{bmatrix} = \frac{\bar{k}(T)A}{\Delta z_j}\begin{bmatrix} 1 & -1 \\ -1 & 1 \end{bmatrix}\begin{bmatrix} T_j \\ T_{j+1} \end{bmatrix} \tag{8}$$

In general, the heat conduction vector is a nonlinear function because the thermal conductivity depends on temperature and Δz_j depends on the surface recession rate. Therefore, an iterative solution procedure is necessary to solve for the time accurate nonlinearities. To aid in the iterative process, it is convenient to linearize the elemental conduction vector with a Taylor series expansion in iteration space according to

$$\begin{bmatrix} \dot{Q}_j \\ \dot{Q}_{j+1} \end{bmatrix}^{v+1} = \begin{bmatrix} \dot{Q}_j \\ \dot{Q}_{j+1} \end{bmatrix}^{v} + \begin{bmatrix} \frac{\partial \dot{Q}_j}{\partial \dot{s}} & \frac{\partial \dot{Q}_j}{\partial T_j} & \frac{\partial \dot{Q}_j}{\partial T_{j+1}} \\ \frac{\partial \dot{Q}_{j+1}}{\partial \dot{s}} & \frac{\partial \dot{Q}_{j+1}}{\partial T_j} & \frac{\partial \dot{Q}_{j+1}}{\partial T_{j+1}} \end{bmatrix}^{v}\begin{bmatrix} \Delta \dot{s} \\ \Delta T_j \\ \Delta T_{j+1} \end{bmatrix}^{v+1} + \cdots \tag{9}$$

Performing the required differentiation for planar geometry gives

$$\begin{aligned}
\frac{\partial \dot{Q}_j}{\partial \dot{s}} &= -\frac{\bar{k}A}{\Delta z_j^2}(T_j - T_{j+1})\frac{\partial \Delta z_j}{\partial \dot{s}} \\
\frac{\partial \dot{Q}_{j+1}}{\partial \dot{s}} &= \frac{\bar{k}A}{\Delta z_j^2}(T_j - T_{j+1})\frac{\partial \Delta z_j}{\partial \dot{s}} \\
\frac{\partial \dot{Q}_j}{\partial T_j} &= \frac{\bar{k}A}{\Delta z_j}\left[1 + \frac{(T_j - T_{j+1})}{2\bar{k}}\left(\frac{\partial k}{\partial T}\right)_j\right] \\
\frac{\partial \dot{Q}_j}{\partial T_{j+1}} &= \frac{\bar{k}A}{\Delta z_j}\left[-1 + \frac{(T_j - T_{j+1})}{2\bar{k}}\left(\frac{\partial k}{\partial T}\right)_{j+1}\right] \\
\frac{\partial \dot{Q}_{j+1}}{\partial T_j} &= \frac{\bar{k}A}{\Delta z_j}\left[-1 - \frac{(T_j - T_{j+1})}{2\bar{k}}\left(\frac{\partial k}{\partial T}\right)_j\right] \\
\frac{\partial \dot{Q}_{j+1}}{\partial T_{j+1}} &= \frac{\bar{k}A}{\Delta z_j}\left[1 - \frac{(T_j - T_{j+1})}{2\bar{k}}\left(\frac{\partial k}{\partial T}\right)_{j+1}\right]
\end{aligned} \tag{10}$$

where $A = 1$ for planar geometry, and

$$\frac{\partial \Delta z_j}{\partial \dot{s}} = \Delta t^{n+1}(\eta_{j+1} - \eta_j) = \Delta t^{n+1}\Delta \eta_j \tag{11}$$

Note that for cylindrical and spherical geometries, the area variation is a function of position $[A = A(z)]$ resulting in additional terms in the surface recession rate sensitivities for all of the terms discussed.

B. Convection

The apparent energy convection rate across a control volume boundary due to boundary translation can be written as

$$\dot{E} = [\rho u e(T) A]_{j+1/2} \tag{12}$$

where $e = h$ for solids, and the specific internal energy can be found from

$$e(T) = e_{\text{ref}} + \int_{T_{\text{ref}}}^{T} C_v(T)\, \mathrm{d}T \tag{13}$$

The corresponding element convection vector, consistent with the established sign convention, is

$$\begin{bmatrix} \dot{E}_j \\ \dot{E}_{j+1} \end{bmatrix} = [\rho u e(T) A]_{j+1/2} \begin{bmatrix} -1 \\ 1 \end{bmatrix} \tag{14}$$

Linearizing the convection vector in iteration space according to a Taylor series expansion gives

$$\begin{bmatrix} \dot{E}_j \\ \dot{E}_{j+1} \end{bmatrix}^{v+1} = \begin{bmatrix} \dot{E}_j \\ \dot{E}_{j+1} \end{bmatrix}^{v} + \begin{bmatrix} \frac{\partial \dot{E}_j}{\partial \dot{s}} & \frac{\partial \dot{E}_j}{\partial T_j} & \frac{\partial \dot{E}_j}{\partial T_{j+1}} \\ \frac{\partial \dot{E}_{j+1}}{\partial \dot{s}} & \frac{\partial \dot{E}_{j+1}}{\partial T_j} & \frac{\partial \dot{E}_{j+1}}{\partial T_{j+1}} \end{bmatrix}^{v} \begin{bmatrix} \Delta \dot{s} \\ \Delta T_j \\ \Delta T_{j+1} \end{bmatrix}^{v+1} + \cdots \tag{15}$$

where the sensitivity matrix entries are

$$\begin{aligned} \frac{\partial \dot{E}_j}{\partial \dot{s}} &= -\overline{\rho\eta} A \bar{e} \\ \frac{\partial \dot{E}_{j+1}}{\partial \dot{s}} &= \overline{\rho\eta} A \bar{e} \\ \frac{\partial \dot{E}_j}{\partial T_j} &= -\frac{1}{2} \bar{\rho}\, \dot{s}\, \bar{\eta} A C_{v_j} \\ \frac{\partial \dot{E}_j}{\partial T_{j+1}} &= -\frac{1}{2} \bar{\rho}\, \dot{s}\, \bar{\eta} A C_{v_{j+1}} \\ \frac{\partial \dot{E}_{j+1}}{\partial T_j} &= \frac{1}{2} \bar{\rho}\, \dot{s}\, \bar{\eta} A C_{v_j} \\ \frac{\partial \dot{E}_{j+1}}{\partial T_{j+1}} &= \frac{1}{2} \bar{\rho}\, \dot{s}\, \bar{\eta} A C_{v_{j+1}} \end{aligned} \tag{16}$$

C. Capacitance

The energy content for an element can be divided into terms corresponding to each of the two subcontrol volumes associated with an element.

$$\begin{bmatrix} \tilde{E}_j \\ \tilde{E}_{j+1} \end{bmatrix} = \begin{bmatrix} \int_{z_j}^{\bar{z}_j} \rho e(T) A\, \mathrm{d}z \\ \int_{\bar{z}_j}^{z_{j+1}} \rho e(T) A\, \mathrm{d}z \end{bmatrix} \tag{17}$$

The internal energy per unit volume in Eq. (17) can be expressed by a Taylor series expansion in position about the element center

$$(\rho e)|_z = \overline{\rho e} + \left.\frac{\partial(\rho e)}{\partial z}\right|_{z=\bar{z}_j} [(z - \bar{z}_j]) + \cdots \tag{18}$$

The elemental energy content vector can now be expressed as

$$\begin{bmatrix} \tilde{E}_j \\ \tilde{E}_{j+1} \end{bmatrix} = \begin{bmatrix} \int_{z_j}^{\bar{z}_j} \left(\overline{\rho e} + \left.\frac{\partial(\rho e)}{\partial z}\right|_{z=\bar{z}_j} (z - \bar{z}_j) \right) A\, \mathrm{d}z \\ \int_{\bar{z}_j}^{z_{j+1}} \left(\overline{\rho e} + \left.\frac{\partial(\rho e)}{\partial z}\right|_{z=\bar{z}_j} (z - \bar{z}_j) \right) A\, \mathrm{d}z \end{bmatrix} \tag{19}$$

To aid in the integration process it is convenient to employ a local coordinate system in which the shape functions are written as

$$\begin{aligned} &N_1(\xi) = \tfrac{1}{2}(1 - \xi) \quad \text{and} \quad N_2(\xi) = \tfrac{1}{2}(1 + \xi) = 1 - N_1(\xi) \\ &\quad \text{for } -1 \le \xi \le 1 \end{aligned} \tag{20}$$

The global coordinate z and local coordinate ξ are related through

$$z = N_1(\xi) z_j + N_2(\xi) z_{j+1} = \bar{z}_j + \frac{\xi}{2} \Delta z_j \tag{21}$$

and consequently the differential length is

$$\mathrm{d}z = \frac{\Delta z_j}{2}\, \mathrm{d}\xi \tag{22}$$

If a finite difference approximation is used for $\partial(\rho e)/\partial z$, the energy capacitance terms can be rewritten in terms of local coordinates as

$$\begin{bmatrix} \tilde{E}_j \\ \tilde{E}_{j+1} \end{bmatrix} = \begin{bmatrix} \overline{\rho e} \frac{\Delta z_j}{2} \int_{-1}^{0} A(\xi)\, \mathrm{d}\xi + [(\rho e)_{j+1} - (\rho e)_j] \frac{\Delta z_j}{4} \int_{-1}^{0} \xi A(\xi)\, \mathrm{d}\xi \\ \overline{\rho e} \frac{\Delta z_j}{2} \int_{0}^{1} A(\xi)\, \mathrm{d}\xi + [(\rho e)_{j+1} - (\rho e)_j] \frac{\Delta z_j}{4} \int_{0}^{1} \xi A(\xi)\, \mathrm{d}\xi \end{bmatrix} \tag{23}$$

Performing the integration for planar geometry gives

$$\begin{bmatrix} \tilde{E}_j \\ \tilde{E}_{j+1} \end{bmatrix} = \frac{A \Delta z_j}{2} \begin{bmatrix} \frac{3}{4} & \frac{1}{4} \\ \frac{1}{4} & \frac{3}{4} \end{bmatrix} \begin{bmatrix} (\rho e)_j \\ (\rho e)_{j+1} \end{bmatrix} \tag{24}$$

The time rate of change of energy content according to an implicit time integrator can be expressed as

$$\frac{\mathrm{d}}{\mathrm{d}t} \begin{bmatrix} \tilde{E}_j \\ \tilde{E}_{j+1} \end{bmatrix}^{v+1} = \frac{1}{\Delta t} \left\{ \begin{bmatrix} \tilde{E}_j \\ \tilde{E}_{j+1} \end{bmatrix}^{v+1} - \begin{bmatrix} \tilde{E}_j \\ \tilde{E}_{j+1} \end{bmatrix}^{n} \right\} \tag{25}$$

and linearizing in iteration space according to a Taylor series expansion gives

$$\frac{\mathrm{d}}{\mathrm{d}t} \begin{bmatrix} \tilde{E}_j \\ \tilde{E}_{j+1} \end{bmatrix}^{v+1} = \frac{1}{\Delta t} \left\{ \begin{bmatrix} \tilde{E}_j \\ \tilde{E}_{j+1} \end{bmatrix}^{v} + \begin{bmatrix} \frac{\partial \tilde{E}_j}{\partial \dot{s}} & \frac{\partial \tilde{E}_j}{\partial T_j} & \frac{\partial \tilde{E}_j}{\partial T_{j+1}} \\ \frac{\partial \tilde{E}_{j+1}}{\partial \dot{s}} & \frac{\partial \tilde{E}_{j+1}}{\partial T_j} & \frac{\partial \tilde{E}_{j+1}}{\partial T_{j+1}} \end{bmatrix}^{v} \begin{bmatrix} \Delta \dot{s} \\ \Delta T_j \\ \Delta T_{j+1} \end{bmatrix}^{v+1} - \begin{bmatrix} \tilde{E}_j \\ \tilde{E}_{j+1} \end{bmatrix}^{n} \right\} \tag{26}$$

where the sensitivity matrix entries are

$$\begin{aligned} \frac{\partial \tilde{E}_j}{\partial \dot{s}} &= A \frac{\partial \Delta z_j}{\partial \dot{s}} \left(\frac{3}{8} (\rho e)_j + \frac{1}{8} (\rho e)_{j+1} \right) \\ \frac{\partial \tilde{E}_{j+1}}{\partial \dot{s}} &= A \frac{\partial \Delta z_j}{\partial \dot{s}} \left(\frac{1}{8} (\rho e)_j + \frac{3}{8} (\rho e)_{j+1} \right) \\ \frac{\partial \tilde{E}_j}{\partial T_j} &= \frac{3 A \Delta z_j}{8} (\rho C_v)_j \\ \frac{\partial \tilde{E}_j}{\partial T_{j+1}} &= \frac{A \Delta z_j}{8} (\rho C_v)_{j+1} \\ \frac{\partial \tilde{E}_{j+1}}{\partial T_j} &= \frac{A \Delta z_j}{8} (\rho C_v)_j \\ \frac{\partial \tilde{E}_{j+1}}{\partial T_{j+1}} &= \frac{3 A \Delta z_j}{8} (\rho C_v)_{j+1} \end{aligned} \tag{27}$$

V. Boundary Conditions

The computer program developed during the current study implemented an element assembly routine common in many finite element programs in which the element sensitivity matrices were merged into a global sensitivity matrix and the application of boundary conditions followed. The general convective/radiative boundary flux, assuming equal diffusion coefficients and no pyrolysis gas rejection, is given by

$$\dot{q}'' = \underbrace{\rho_e u_e C_{h_o}\left(\frac{C_h}{C_{h_o}}\right)(h_w - h_r)}_{\text{aerodynamic heating}} + \underbrace{\epsilon\sigma\left(T_w^4 - T_{\text{res}}^4\right)}_{\text{radiation}} + \underbrace{\dot{m}'' h_w}_{\text{ablation}} \quad (28)$$

where the heat transfer coefficient ($\rho_e u_e C_{h_o}$), recovery enthalpy, and reservoir temperature are time dependent and supplied by the user. The wall gas enthalpy will be determined using two different ablation models, but first the aerodynamic heating and radiative boundary fluxes will be discussed.

A. Aerodynamic Heating Flux

The aerodynamic heating flux in Eq. (28) is given by

$$\dot{q}''_{\text{ah}} = \rho_e u_e C_{h_o}\left(\frac{C_h}{C_{h_o}}\right)(h_w - h_r) \quad (29)$$

where the code inputs include the recovery enthalpy (h_r), heat transfer coefficient ($\rho_e u_e C_{h_o}$), pressure, edge velocity (u_e), specification of laminar or turbulent flow, and tabulated surface thermochemistry data. The code developed in the current study includes optional corrections to the Stanton number for both wall temperature and blowing effects. In the case of uncoupled flowfield and thermal response solutions, the computational fluid dynamics (CFD) wall boundary condition may be an isothermal or equilibrium condition which ignores conduction into the body in the surface energy balance. In this case, corrections to the Stanton number should be applied to account for inconsistent wall temperatures between the flowfield and thermal response solutions. The form of the total Stanton number correction is given by

$$\frac{C_h}{C_{h_o}} = \Omega_{\text{hw}}\Omega_{\text{blw}} \quad (30)$$

Note that the combined Stanton number correction model assumes that the wall temperature and blowing corrections are independent of each other, and they can therefore be applied either separately or in the multiplicative fashion in Eq. (30).

1. Blowing Correction

Mass injection into the flowfield is known to thicken the boundary layer, and it has a cooling effect relative to a nonblowing case resulting from a decrease in the convective heat transfer. The blowing correction, as presented by Kays et al. [12], is

$$\Omega_{\text{blw}} = \frac{\Phi}{e^{\Phi} - 1} \quad (31)$$

where

$$\Phi = 2\lambda\frac{\dot{m}''}{\rho_e u_e C_{h_o}} \quad (32)$$

and

$$\dot{m}'' = \rho\dot{s} \quad (33)$$

for nondecomposing materials. The blowing reduction parameter used in this study is 0.5 for laminar flow and 0.4 for turbulent flow. The blowing correction sensitivities are given by

$$\frac{\partial\Omega_{\text{blw}}}{\partial\dot{s}} = \frac{(\partial\Phi/\partial\dot{s})[e^{\Phi}(1-\Phi) - 1]}{(e^{\Phi} - 1)^2} \quad (34)$$

and

$$\frac{\partial\Omega_{\text{blw}}}{\partial T} = 0 \quad (35)$$

where

$$\frac{\partial\Phi}{\partial\dot{s}} = \frac{2\lambda\rho}{\rho_e u_e C_{h_o}} \quad (36)$$

It should be noted that the Stanton number reduction due to mass injection does have a dependence on the properties of the injected and boundary layer gases [12–14]. Equation (31) has been used in practice for graphite ablation in an air boundary layer, where the molecular weight difference between the injected and boundary layer gases is not significant. However, it should not be used for helium or hydrogen injection into air.

2. Wall Temperature Correction

For the wall temperature correction, one of two methods is used depending on whether the flow is laminar or turbulent. For laminar and stagnation point flows, the method presented by Cohen and Reshotko [15] is used and is given by

$$\Omega_{\text{hw}} = \left(\frac{\rho_{\text{hw}}\mu_{\text{hw}}}{\rho_{\text{cw}}\mu_{\text{cw}}}\right)^{0.1} \quad (37)$$

For this method, the gas density and viscosity at both the hot and the cold wall conditions must be obtained. The "cold wall" nomenclature is used to denote the wall condition with respect to the flowfield solution boundary condition whether it be isothermal or an equilibrium condition. For simulations where air is the flowfield gas, the code developed during the current study contains tabulated functions of temperature, enthalpy, molecular weight, viscosity, and Prandtl number at several pressures. Therefore pressure and any one of the other tabulated properties can be chosen as the independent variables when interpolating in these tables. As a result, the tabulated data in conjunction with the perfect gas law can be used to determine the laminar wall temperature correction in Eq. (37) when the cold wall temperature and pressure are provided.

For turbulent flows, a correction based on Eckert's reference enthalpy method [16,17] is used:

$$\Omega_{\text{hw}} = \left(\frac{\mu^*_{\text{hw}}}{\mu^*_{\text{cw}}}\right)^{0.2}\left(\frac{\rho^*_{\text{hw}}}{\rho^*_{\text{cw}}}\right)^{0.8} \quad (38)$$

The reference properties in Eq. (38) are calculated from the tabulated data mentioned above given the pressure and reference enthalpies

$$h^*_{\text{hw}} = \tfrac{1}{2}(h_e + h_{\text{hw}}) + 0.11 r u_e^2 \quad (39)$$

and

$$h^*_{\text{cw}} = \tfrac{1}{2}(h_e + h_{\text{cw}}) + 0.11 r u_e^2 \quad (40)$$

where

$$h_e = h_r - r\frac{u_e^2}{2} \quad (41)$$

The recovery factor can be found from

$$r = Pr_{\text{hw}}^{1/3} \quad (42)$$

Because of the complexity of the wall temperature correction, its sensitivity to temperature is determined from a central finite difference by means of perturbation of the boundary temperature. Thus

$$\frac{\partial\Omega_{\text{hw}}}{\partial T} = \frac{\Omega_{\text{hw}}(T_w + \delta) - \Omega_{\text{hw}}(T_w - \delta)}{2\delta} \quad (43)$$

where

$$\delta = T_w \times 10^{-8} \tag{44}$$

The wall temperature correction factor has no recession rate dependence giving

$$\frac{\partial \Omega_{\text{hw}}}{\partial \dot{s}} = 0 \tag{45}$$

3. Aerodynamic Heating Sensitivities

The aerodynamic heating flux's sensitivities are given by

$$\frac{\partial \dot{q}''_{\text{ah}}}{\partial T} = \rho_e u_e C_{h_o} \left\{ \left[\frac{C_h}{C_{h_o}} \right] \frac{\partial h_w}{\partial T} \bigg|_{T=T_w} + (h_w - h_r) \frac{\partial}{\partial T} \left[\frac{C_h}{C_{h_o}} \right] \right\} \tag{46}$$

and

$$\frac{\partial \dot{q}''_{\text{ah}}}{\partial \dot{s}} = \rho_e u_e C_{h_o} (h_w - h_r) \frac{\partial}{\partial \dot{s}} \left[\frac{C_h}{C_{h_o}} \right] \tag{47}$$

where

$$\frac{\partial}{\partial T} \left[\frac{C_h}{C_{h_o}} \right] = \Omega_{\text{blw}} \frac{\partial \Omega_{\text{hw}}}{\partial T} \tag{48}$$

and

$$\frac{\partial}{\partial \dot{s}} \left[\frac{C_h}{C_{h_o}} \right] = \Omega_{\text{hw}} \frac{\partial \Omega_{\text{blw}}}{\partial \dot{s}} \tag{49}$$

The wall gas enthalpy's sensitivity to temperature is found with a finite difference from the tabulated thermochemistry data. For the general in-depth decomposition case, the wall gas enthalpy is also a function of the surface recession rate and the corresponding sensitivity must be accounted for.

B. Radiative Flux

The radiative flux in Eq. (28) is given by

$$\dot{q}''_{\text{rad}} = \epsilon \sigma \left(T_w^4 - T_{\text{res}}^4 \right) \tag{50}$$

and the sensitivities are simply

$$\frac{\partial \dot{q}''_{\text{rad}}}{\partial \dot{s}} = 0 \tag{51}$$

and

$$\frac{\partial \dot{q}''_{\text{rad}}}{\partial T} = 4\epsilon \sigma T_w^3 + \frac{\partial \epsilon}{\partial T} \bigg|_{T=T_w} \left(T_w^4 - T_{\text{res}}^4 \right) \sigma \tag{52}$$

C. Ablation Models

1. Heat of Ablation (Q^*)

The heat of the ablation model assumes that ablation occurs at a fixed temperature and that there is a fixed amount of energy consumed per unit mass of ablated material, which is given by

$$Q^* = h_w - h_s = h_w - \left[e_{\text{ref}} + \int_{T_{\text{ref}}}^{T_{\text{abl}}} C_v(T)\, \mathrm{d}T \right] \tag{53}$$

As a result, the enthalpy associated with the material being convected out of the surface control volume is

$$h_w = h_s + Q^* \tag{54}$$

The energy flux resulting from the ablative process is

$$\dot{q}''_{\text{abl}} = \rho \dot{s} h_w \tag{55}$$

and the resulting sensitivities are

$$\frac{\partial \dot{q}''_{\text{abl}}}{\partial \dot{s}} = \rho h_w \tag{56}$$

and

$$\frac{\partial \dot{q}''_{\text{abl}}}{\partial T} = \rho \dot{s} \frac{\partial h_s}{\partial T} \bigg|_{T=T_w} = \rho \dot{s} C_p(T_w) \tag{57}$$

Note that a weakness of the heat of the ablation model is that the wall gas enthalpy in the ablative flux is different from the wall gas enthalpy in the aerodynamic heating flux which is determined from nonablating thermochemistry data. In addition, the heat of the ablation model cannot be accurately applied to pyrolyzing ablators because it does not account for a variable wall temperature and pyrolysis gas effects at the surface.

In spite of the weaknesses from a physical modeling perspective, there are two primary reasons for including the heat of ablation discussion. First, the formal verification process requires a systematic verification of each of the terms in the model equations. Because analytical solutions are known for heat of ablation problems, it was concluded that including this model was a logical way of verifying the grid convection term in the governing equation. Second, this model is still commonly used by analysts to provide quick preliminary analyses of new materials whose properties have not been thoroughly characterized.

2. Thermochemical Ablation

The thermochemical ablation model used in the current study is the same as described by Moyer and Rindal [1]. The basic assumption of this model is that the gaseous ablation products are in thermal and chemical equilibrium with the boundary layer gases at the wall temperature and pressure. It should be noted that a finite-rate chemistry model may more accurately describe the wall conditions, but the chemical equilibrium model is still commonly used for heat-shield designs.

Like the heat of the ablation model, the ablative flux in the thermochemical model is given by Eq. (55), but now the wall gas enthalpy is a function of surface temperature and pressure which is tabulated in the input thermochemical data. Therefore, for nondecomposing materials, Eq. (56) is still valid for thermochemical ablation, but Eq. (57) is not. The ablative flux's sensitivity to temperature is given by

$$\frac{\partial \dot{q}''_{\text{abl}}}{\partial T} = \rho \dot{s} \frac{\partial h_w}{\partial T} \bigg|_{T=T_w} \tag{58}$$

where $\partial h_w / \partial T$ is found with a finite difference from the tabulated thermochemistry data as previously mentioned. The auxiliary relationship for thermochemical ablation gives the zeroth residual equation

$$R_0 = \frac{\rho \dot{s}}{\rho_e u_e C_h} \frac{C_h}{C_m} - B'_c = 0 \tag{59}$$

where the dimensionless ablation rate is tabulated in the thermochemical data and C_h / C_m is an input parameter. The sensitivities of the residual to temperature and surface recession rate are given by

$$\frac{\partial R_0}{\partial T} = \frac{-\rho \dot{s}}{\rho_e u_e C_m (C_h / C_{h_o})} \frac{\partial (C_h / C_{h_o})}{\partial T} - \frac{\partial B'_c}{\partial T} \tag{60}$$

and

$$\frac{\partial R_0}{\partial \dot{s}} = \frac{\rho}{\rho_e u_e C_m} \left[1 - \frac{\dot{s}}{C_h / C_{h_o}} \frac{\partial (C_h / C_{h_o})}{\partial \dot{s}} \right] \tag{61}$$

where $\partial B'_c / \partial T$ is found with a finite difference from the tabulated thermochemistry data. Note that for decomposing materials, the dimensionless char ablation rate and wall gas enthalpy have

functional dependencies on the surface recession rate in addition to the temperature.

VI. Verification Results

A. Transient Conduction with Variable Properties and No Ablation

1. Problem Statement

Consider a one-dimensional uniform density planar slab subject to a constant specified heat flux on the front face and an adiabatic back face. The governing equation, boundary conditions, and initial conditions that characterize the problem are

$$\rho C_v \frac{\partial T}{\partial t} = \frac{\partial}{\partial z}\left(k\frac{\partial T}{\partial z}\right) \quad \text{for } 0 \le z \le L \qquad -k\frac{\partial T}{\partial z}\bigg|_{z=0} = \dot{q}''$$
$$-k\frac{\partial T}{\partial z}\bigg|_{z=L} = 0 \qquad T(z, t=0) = T_o \tag{62}$$

and the parameters for this problem are given in Table 1. The thermal conductivity and specific heat are given in Table 2 and are assumed to vary linearly with temperature while the thermal diffusivity is constant giving

$$k(T) = k_1 + \frac{k_2 - k_1}{T_2 - T_1}(T - T_1) \tag{63}$$

$$C_v(T) = C_{v,1} + \frac{C_{v,2} - C_{v,1}}{T_2 - T_1}(T - T_1) \tag{64}$$

$$\alpha = \frac{k_1}{\rho C_{v,1}} = \frac{k_2}{\rho C_{v,2}} \tag{65}$$

2. Analytical Solution

The analytical solution to this problem can be found by first applying Kirchoff's transformation

$$\theta = \frac{1}{k_{\text{ref}}}\int_{T_{\text{ref}}}^{T} k(\hat{T})\, \mathrm{d}\hat{T} \tag{66}$$

and then using the related constant property solution as described by Arpaci [18]. Performing the integration with $T_{\text{ref}} = T_1$ and $k_{\text{ref}} = k_1$ gives

$$\theta = (T - T_1) + \frac{k_2 - k_1}{T_2 - T_1}\frac{1}{2k_1}(T - T_1)^2 \tag{67}$$

The above equation is quadratic in $(T - T_1)$, and can be solved to yield

Table 1 Variable property verification problem parameters

$T_o = 300$ K
$\dot{q}'' = 7.5 \times 10^5$ W/m^2
$L = 0.01$ m
$\rho = 8000$ kg/m^2
$\alpha = k/(\rho C_v) = 2.5 \times 10^{-6}$ m^2/s

Table 2 Temperature-dependent properties for variable property verification problem

T, K	k, W/m · K	C_v, J/kg · K
$T_1 = 300$	10	500
$T_2 = 1300$	100	5000

$$T - T_1 = (T_2 - T_1)\left(\frac{k_1}{k_2 - k_1}\right)\left[-1 \pm \sqrt{1 + \frac{2\theta}{T_2 - T_1}\left(\frac{k_2 - k_1}{k_1}\right)}\right] \tag{68}$$

where the physically meaningful root is denoted by the plus sign since

$$T > T_1 \quad \text{when} \quad \frac{k_2 - k_1}{T_2 - T_1} > 0$$

The transformed energy equation, boundary conditions, and initial conditions become

$$\frac{\partial \theta}{\partial t} = \alpha\frac{\partial^2 \theta}{\partial z^2} \quad \text{for } 0 \le z \le L \qquad -k_1\frac{\partial \theta}{\partial z}\bigg|_{z=0} = \dot{q}''$$
$$-k_1\frac{\partial \theta}{\partial z}\bigg|_{z=L} = 0 \qquad \theta(z, t=0) = \theta_o = \theta(T = T_o) \tag{69}$$

The transformed energy equation now has the same form as the related constant property case, and the analytical solution is

$$\frac{\theta(z,t) - \theta_o}{\dot{q}'' L/k_1} = \frac{\alpha t}{L^2} + \frac{1}{3} - \frac{z}{L} + \frac{1}{2}\left(\frac{z}{L}\right)^2 - \frac{2}{\pi^2}\sum_{n=1}^{\infty}\frac{1}{n^2}\exp\left(-n^2\pi^2\frac{\alpha t}{L^2}\right)\cos\left(n\pi\frac{z}{L}\right) \tag{70}$$

3. Grid Refinement and Nonlinear Convergence Studies

The domain was discretized with four different uniform grids denoted by coarse, medium, fine, and extra fine. The coarse grid had 10 uniform elements while each subsequent grid doubled the number of elements thereby halving the mesh spacing. Because the implicit time integrator is expected to be first order and the spatial discretization is expected to be second order, it will be assumed that the discretization error (DE) can be expressed as

$$\text{DE} = a\Delta t + b\Delta x^2 + (\text{higher order terms}) \tag{71}$$

Factoring out a $b\Delta x^2$ and ignoring the higher order terms gives

$$\text{DE} = b\Delta x^2\left(1 + \frac{a\Delta t}{b\Delta x^2}\right) \tag{72}$$

As a result, if the spatial and temporal grids are simultaneously refined while keeping $\Delta t/\Delta x^2$ constant, then the spatial and temporal orders of accuracy can be confirmed if the grid convergence is second order. The grid parameters for the four grids with $\alpha\Delta t/\Delta x^2 = 1.25$ can be seen in Table 3. Figure 4 shows that the solutions at both 4 and 40 s exhibit second-order grid convergence.

Theoretically, a correct implementation of a full Newton's method for a system of equations should exhibit second-order nonlinear convergence. If the method converges at a rate other than second order, then it is likely that a mistake exists in the derivation or implementation. The error relationship for successive iterations is given by

$$(\text{error})^{\nu+1} = a[(\text{error})^{\nu}]^2 \tag{73}$$

Therefore a plot of $\log|(\text{error})^{\nu+1}|$ versus $\log|(\text{error})^{\nu}|$ should result

Table 3 Parameters for variable property problem grid refinement study

Grid	No. elements	Δx, m	Δt, s
Coarse	10	0.001	0.5
Medium	20	0.0005	0.125
Fine	40	0.00025	0.03125
Extra fine	80	0.000125	0.0078125

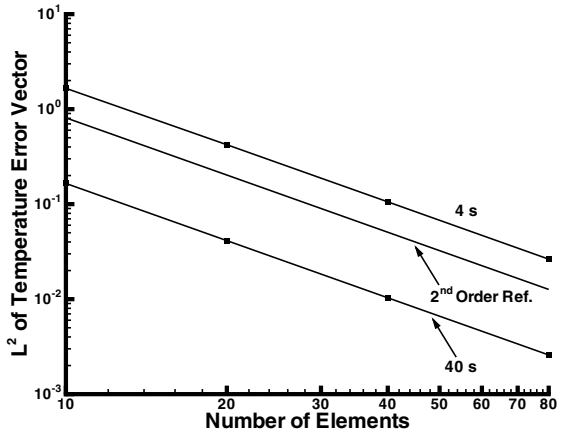

Fig. 4 Grid refinement study for variable property verification problem.

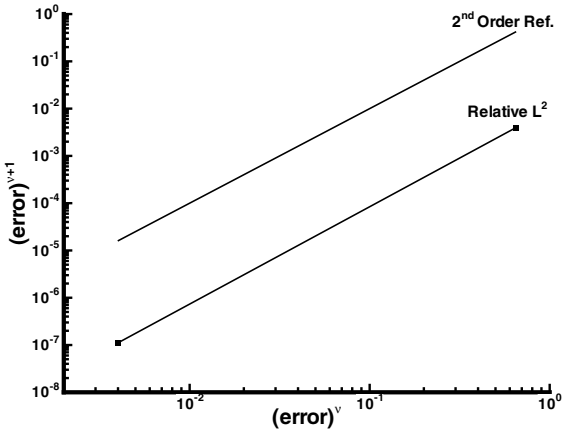

Fig. 5 Nonlinear convergence rate for variable property verification problem.

in a line with a slope of 2 if the method is correctly implemented [19]. Because the Newton solver will converge to the analytical solution plus discretization error, the difference in L^2 of the temperature error vector between the current iteration and the converged solution is used as the error metric:

$$(\text{error})^{\nu} = (L^2)^{\nu} - (L^2)^{\text{converged}} \tag{74}$$

As a result, there are no data points for the final two iterations of a time step because this will result in coordinates with zero values which compromise the value of the logarithmic plot. Figure 5 shows the second-order nonlinear convergence rate for a single time step that had a total of four iterations.

B. Q^* Ablation with Blowing Correction

1. Problem Statement

Consider a one-dimensional, uniform density, ablative, semi-infinite, planar slab with constant material properties and isothermal boundaries. The governing equation and boundary conditions that characterize the problem are

$$k\frac{\mathrm{d}^2T}{\mathrm{d}x^2} + \rho\dot{s}C_v\frac{\mathrm{d}T}{\mathrm{d}x} = 0$$
$$T(x=0) = T_{\text{abl}}$$
$$T(x=\infty) = T_o \tag{75}$$

and the material properties and problem parameters are given in Table 4. Although the differential equation assumes there is a boundary at $x = \infty$, the corresponding numerical simulation must be for a finite computational domain. For consistency between the numerical and analytical solutions, the computational domain must be chosen sufficiently large for the semi-infinite assumption to be valid.

Table 4 Q^* verification problem parameters

$k = 0.2\ \text{W/m} \cdot \text{K}$
$\rho = 2000\ \text{kg/m}^3$
$C_v = 1000\ \text{J/kg} \cdot \text{K}$
$L = 3.0 \times 10^{-2}\ \text{m}$
$Q^* = 2 \times 10^6\ \text{J/kg}$
$\dot{q}'' = 2 \times 10^6\ \text{W/m}^2$
$\dot{s} = 4.0 \times 10^{-4}\ \text{m/s}$
$T_{\text{abl}} = 800\ \text{K}$
$T_o = T_{\text{ref}} = 300\ \text{K}$

2. Analytical Solution

The analytical solution to Eq. (75) is

$$\frac{T(x) - T_o}{T_{\text{abl}} - T_o} = \exp(-\dot{s}x/\alpha) \tag{76}$$

The steady-state temperature profile with respect to the x-coordinate system translates through the remaining material as the ablation front moves. The surface energy balance can be written as

$$-k\left.\frac{\mathrm{d}T}{\mathrm{d}x}\right|_{x=0} = \dot{q}'' - \rho\dot{s}Q^* \tag{77}$$

and substituting the analytical temperature profile into the surface energy balance gives the necessary heat flux found in Table 4:

$$\dot{q}'' = \rho\dot{s}[C_v(T_{\text{abl}} - T_o) + Q^*] \tag{78}$$

To use this as a verification problem, the procedure is to numerically solve a problem with a specified heat flux on the front face and a nonuniform initial temperature profile given by Eq. (76) and see how well the computed surface recession rate compares to the known recession rate given in Table 4.

The aerodynamic heating boundary flux with blowing correction is given by

$$\dot{q}'' = \rho_e u_e C_{h_o} \Omega_{\text{blw}}(h_w - h_r) \tag{79}$$

The gas enthalpy model adopted for this verification problem is a constant specific heat (corresponding to air) and is given as

$$h_w(T) = C_{p_w}(T - T_{\text{ref}}) \tag{80}$$

where

$$C_{p_w} = 1.00416 \times 10^3\ \text{J/kg} \cdot \text{K}$$

It will be assumed that the recovery temperature of the boundary layer edge gases is 1800 K, and the corresponding recovery enthalpy is

$$h_r(T_r = 1800\ \text{K}) = 1.506240 \times 10^6\ \text{J/kg}$$

While ablation is taking place, $T_w = T_{\text{abl}} = 800$ K with a corresponding enthalpy of

$$h_w(T_w = 800\ \text{K}) = 5.02080 \times 10^5\ \text{J/kg}$$

The corrected heat transfer coefficient can now be determined from Eq. (79) and is found to be

$$\rho_e u_e C_h = 1.9917145\ \text{kg/m}^2 \cdot \text{s}$$

If the laminar blowing correction is used, the uncorrected heat transfer coefficient is

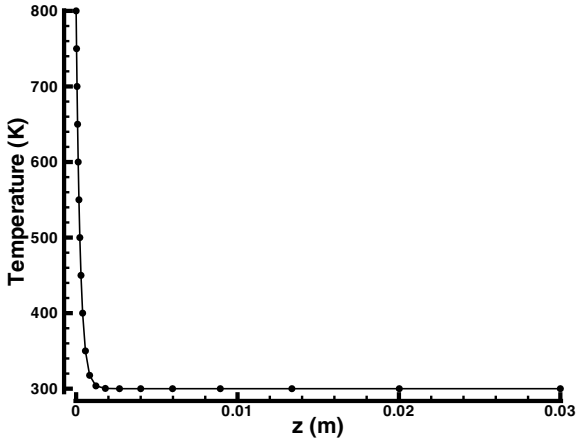

Fig. 6 Initial temperature profile on the 19-element grid.

$$\rho_e u_e C_{h_o} = 2.3692465 \text{ kg/m}^2 \cdot \text{s}$$

An aerodynamic heating flux and thermochemistry data with the above values for $\rho_e u_e C_{h_o}$, h_r, C_{p_w}, and h_w is imposed on the ablating surface while the other boundary condition for the numerical model is adiabatic.

3. Grid Refinement and Nonlinear Convergence Studies

The problem was solved using three different grids designated as coarse, medium, and fine. Each grid is nonuniform and is based on an exponential grid with a geometric progression modification. The motivation behind the piecewise nonuniform grid technique is as follows:

1) Realistic uniform grids for which the method is known to be second order spatially were inadequate to ensure the results were in the asymptotic regime. Several uniform grids were tried, and although they could capture the steep gradients, the location of the largest error typically was at the back face where no activity is supposed to be happening.

2) A nonuniform grid, which would be expected to do a better job of capturing the steep gradients, is not necessarily second order spatially. Because the profile is exponential, several exponentially stretched grids were tried in which the initial temperature drop between nodes was constant. Again, the largest temperature error tended to be at the back face, and the errors were never in the asymptotic regime.

3) Next, a modified exponential grid was devised. For a 10 element exponential grid, the 10th element was replaced by 10 more elements in an expanding sequence based on a geometric progression with $\Delta x_{j+1}/\Delta x_j = 1.5$. The resulting grid and initial conditions are shown in Fig. 6. The sequence of grid refinements was accomplished by taking the 19-element baseline grid given in Fig. 6 and successively dividing each element in half. This process was repeated so that a total of three grids was produced. Similar grid refinement studies for nonuniform grids have been performed by Blottner [20,21].

The time step was determined by keeping the grid scale Fourier number based on the first element thickness ($\alpha \Delta t/\Delta x_1^2$) constant at 1.44133. The grid parameters are given in Table 5, and the grid refinement study which shows second-order convergence in both the predicted temperature profile and recession rate can be seen in Fig. 7.

Table 5 Parameters for Q^* ablation problem grid refinement study

Grid	No. elements	Δx_1, m	Δt, s
Coarse	19	2.6340×10^{-5}	0.01
Medium	38	1.3170×10^{-5}	0.0025
Fine	76	6.5850×10^{-6}	0.000625

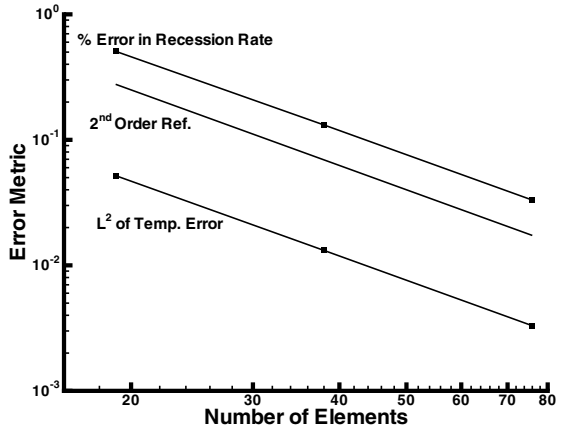

Fig. 7 Grid refinement study for Q^* ablation verification problem.

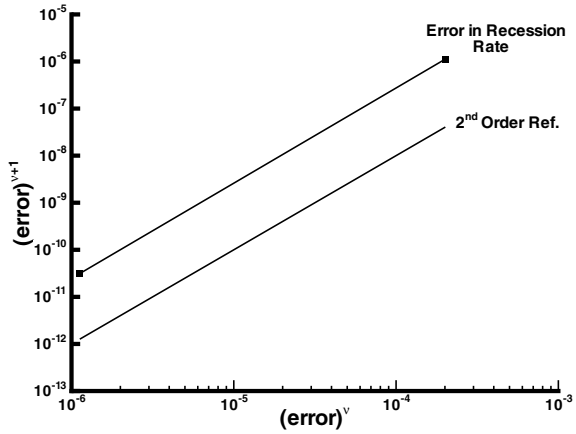

Fig. 8 Nonlinear convergence of surface recession rate for Q^* ablation verification problem.

The nonlinear convergence rate for the Q^* model was determined by using the difference in the surface recession rate between the current iteration and the converged solution as the error metric, and the results shown in Fig. 8 confirm the second-order convergence rate.

$$(\text{error})^v = \dot{s}^v - \dot{s}^{\text{converged}} \tag{81}$$

C. Thermochemical Ablation

Because of the complexity of determining an analytical solution to a thermochemical ablation problem with Stanton number corrections, Richardson extrapolation as described by Roache [22] was used to confirm the spatial order of accuracy of the thermochemical ablation solution procedure. For this process, a 0.5 in. domain was discretized with a series of four uniform grids which are denoted by coarse, medium, fine, and extra fine. The grid parameters can be seen in Table 6 where $\Delta t/\Delta x^2 = 1000$ s/in.^{2}. If it is assumed that the discretization method is second order spatially and that the two grids used to generate the solutions for the extrapolation procedure have the relationship

Table 6 Parameters for thermochemical ablation problem grid refinement study

Grid	No. elements	Δx, in.	Δt, s
Coarse	50	0.01	0.1
Medium	100	0.005	0.025
Fine	200	0.0025	0.00625
Extra fine	400	0.00125	0.0015625

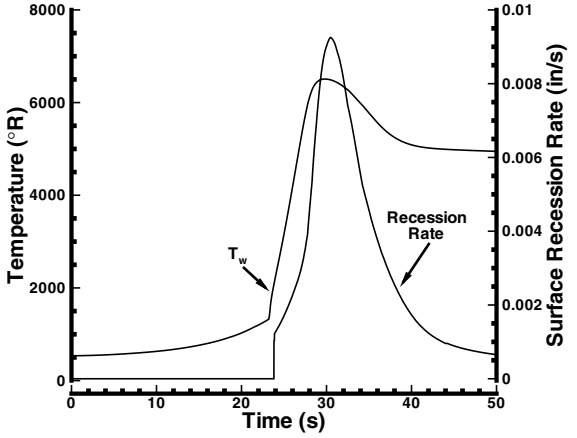

Fig. 9 Surface temperature and recession rate histories for thermochemical ablation verification problem.

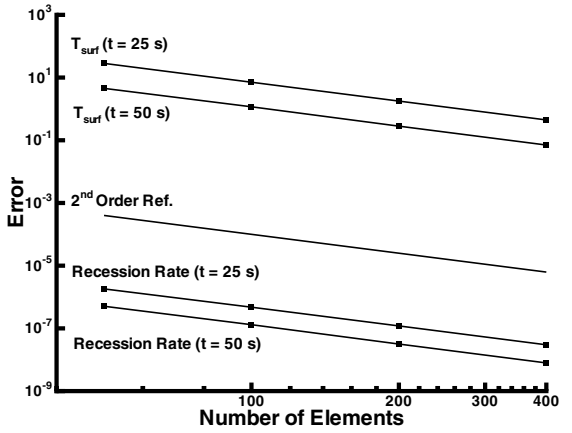

Fig. 10 Richardson extrapolation grid convergence results for thermochemical ablation verification problem.

$$\frac{\Delta x_{\text{fine}}}{\Delta x_{\text{extra fine}}} = 2 \tag{82}$$

then the exact solution can be approximated by

$$f_{\text{exact}} \cong \frac{4}{3} f_{\text{extra fine}} - \frac{1}{3} f_{\text{fine}} \tag{83}$$

The approximation of the exact solution is fourth order accurate if the two solutions used in the extrapolation are second order accurate. This procedure was performed on the surface temperature and surface recession rate for a carbon–carbon ablation problem with a typical ballistic reentry trajectory for which the surface temperature and recession rate histories are shown in Fig. 9. The errors in surface temperature and recession rate were then computed at $t = 25$ s and 50 s for each of the four grids. If the error reduction for the coarse and medium grids is colinear with the error reduction for the fine and extra-fine grids, then the second-order accuracy of the scheme can be confirmed. Figure 10 shows that the scheme, in fact, exhibits second-order grid convergence for both error metrics.

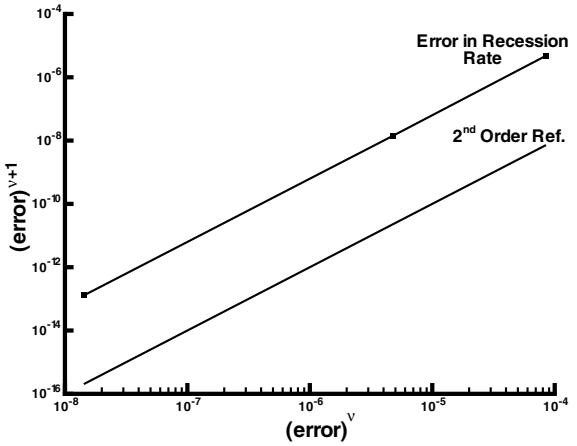

Fig. 11 Nonlinear convergence of surface recession rate for thermochemical ablation verification problem.

Table 7 Grid parameters for spatial refinement

No. elements	Δx, m	Δt, s
20	1.5×10^{-3}	0.01
40	7.5×10^{-4}	0.01
80	3.75×10^{-4}	0.01
160	1.875×10^{-4}	0.01
320	9.375×10^{-5}	0.01
640	4.6875×10^{-5}	0.01

The nonlinear convergence rate was determined for the thermochemical ablation problem using the same error metric described in Eq. (81), and the second-order results can be seen in Fig. 11.

VII. Timing Study

When ablation is occurring, the global sensitivity matrix includes recession rate sensitivities associated with the residual equation at each node. The resulting linear system takes the following form:

$$\begin{bmatrix} e_0 & c_0 & 0 & 0 & 0 & 0 \\ e_1 & b_1 & c_1 & 0 & 0 & 0 \\ e_2 & a_2 & b_2 & c_2 & 0 & 0 \\ e_3 & 0 & a_3 & b_3 & c_3 & 0 \\ e_4 & 0 & 0 & a_4 & b_4 & c_4 \\ e_5 & 0 & 0 & 0 & a_5 & b_5 \end{bmatrix}^{\nu} \begin{bmatrix} \Delta \dot{s} \\ \Delta T_1 \\ \Delta T_2 \\ \Delta T_3 \\ \Delta T_4 \\ \Delta T_5 \end{bmatrix}^{\nu+1} = \begin{bmatrix} d_0 \\ d_1 \\ d_2 \\ d_3 \\ d_4 \\ d_5 \end{bmatrix}^{\nu} \tag{84}$$

where the domain is composed of five nodes for this specific case. An algorithm was developed to solve this system by eliminating the superdiagonal using Gaussian elimination followed by back-substitution to determine the correction vector [10]. For simulations that have both ablating and nonablating intervals, the code switches between a tridiagonal solver and the new linear system solver to minimize computational time.

A. Complete Sensitivity Matrix vs Tridiagonal Formulation

A timing study was performed to determine the advantage of including the entire sensitivity matrix versus only including the tridiagonal terms. Experience has shown that both methods converge to the same solution, but the tridiagonal system exhibits first-order

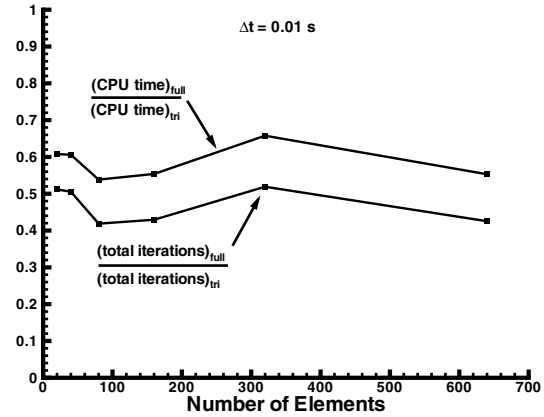

Fig. 12 Timing study results for the spatial grid refinement on the Q^* ablation verification problem.

Table 8 Grid parameters for temporal refinement.

Δt, s	No. elements	Δx, m
0.01	20	1.5×10^{-3}
0.005	20	1.5×10^{-3}
0.0025	20	1.5×10^{-3}
0.00125	20	1.5×10^{-3}

iterative convergence. Consequently, it is of interest to determine if the extra development, verification, and computational time necessary to calculate the entire recession rate sensitivity vector benefits the analyst.

For the Q^* ablation verification problem the spatial and temporal grids were refined separately to isolate the effects of each refinement. The parameters for the uniform grids used in the spatial refinement study are given in Table 7, and the results can be seen in Fig. 12. The parameters and results for the temporal grid refinement timing study are given in Table 8 and Fig. 13, respectively. It is evident that including the entire sensitivity matrix provides a reduction in overall computational time although it is about 19 to 30% slower per iteration (increases as the mesh is refined) than the tridiagonal formulation for the given problem.

B. Nonlinear Iteration vs Material Property Lagging

It is also of interest to determine if iterating on the entire system of equations saves computational time when compared to the commonly used material property lagging approach. The variable property verification problem was solved on all four spatial grids in Table 3 for both approaches to compare the computational time necessary to give equally accurate solutions. The time step for the iterative method solutions was chosen to be 0.5 s for each grid, and the L^2 of the temperature error vector was calculated at the final time. The time step for the lagging method solutions was varied until the desired accuracy was achieved on each grid, and the results can be seen in Fig. 14. It can be seen that there is a second-order relationship between grid refinement and computational time savings to achieve the same accuracy for the variable property problem. As a result, for a given accuracy requirement using the iterative solution procedure as opposed to the lagging method can significantly decrease the

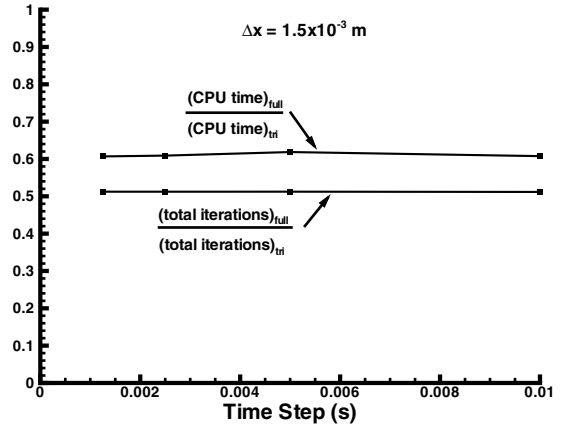

Fig. 13 Timing study results for temporal grid refinement on the Q^* ablation verification problem.

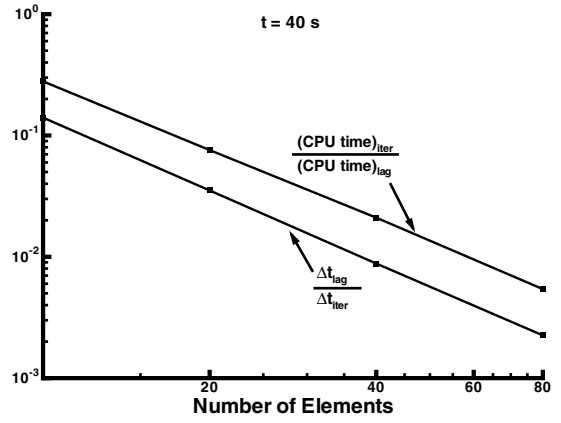

Fig. 14 Timing study comparing iterative and lagging methods for variable property verification problem.

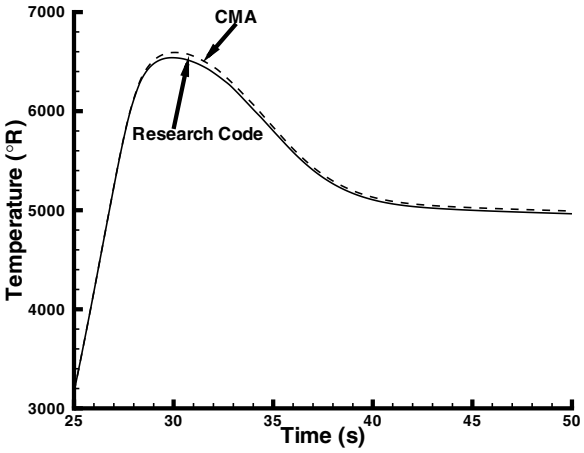

Fig. 15 Comparison of surface temperature predictions for the thermochemical ablation verification problem.

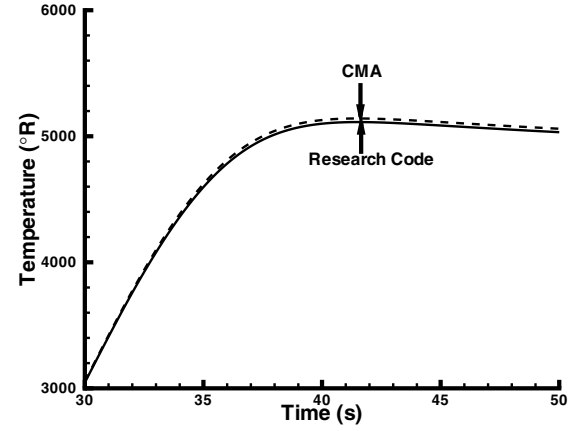

Fig. 16 Comparison of back boundary temperature predictions for the thermochemical ablation verification problem.

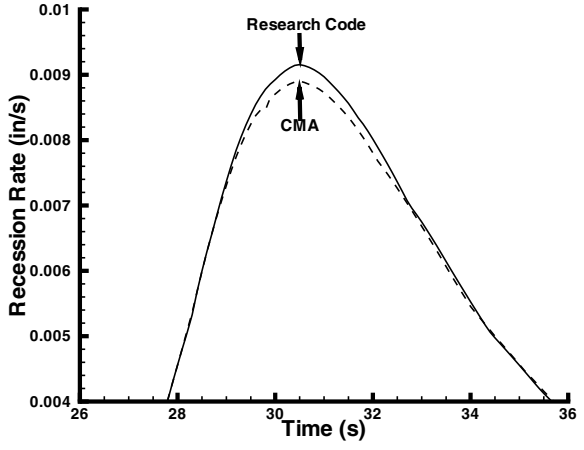

Fig. 17 Comparison of recession rate predictions for the thermochemical ablation verification problem.

Table 9 Peak value comparison for the research code and CMA

Peak value in research code	CMA % difference
$T_s = 6508$ °R at 29.8 s	1.29 at 30.1 s
$T_{back} = 5094$ °R at 41.5 s	0.93 at 41.5 s
$\dot{s} = 9.251 \times 10^{-3}$ in./s at 30.5 s	−3.85 at 30.5 s

computational time necessary to find solutions (especially on relatively fine grids) because larger time steps can be used.

VIII. Code-to-Code Comparison

The thermochemical ablation verification problem was solved on the medium grid in Table 6 using CMA and the code developed during the current study for a consistency check with an established code. It is important to note that the major differences between the codes are as follows:

1) CMA uses a translating/node-dropping grid scheme.

2) CMA iterates only on the surface energy balance and lags temperature-dependent properties and surface recession rate for the interior node solution.

3) CMA uses a lumped capacitance method while the research code uses a distributed capacitance method.

Figures 15–17 compare the predictions from the two codes for surface temperature, back boundary temperature, and recession rate, respectively, and Table 9 shows the relative difference between the two predictions at the peak values.

It is evident that the two programs have good agreement which gives additional indication that the method has been implemented correctly. The largest discrepancy is at the time of the peak surface recession rate where the research code predicts a higher recession rate than CMA. However, the results do not suggest which difference in the models is causing this discrepancy or if this is a combined effect of several of the differences. It should be noted that each of the differences mentioned above provides improved accuracy over CMA. The advantages of items 1 and 2 are discussed in Secs. III and VII.B, while a distributed capacitance method is advantageous over a lumped capacitance method because a temperature variation within each element is accounted for.

IX. Conclusions

A one-dimensional ablative thermal response code with a contracting grid scheme has been developed and verified to exhibit second-order spatial accuracy and first-order temporal accuracy for temperature-dependent properties, heat of ablation, and thermochemical ablation problems. Newton's method for the entire system of equations has been implemented and has also been verified to exhibit second-order nonlinear convergence rates for the verification suite. The model has shown good agreement with CMA, but it also includes several improvements in the solution procedure. Iterating on the entire system of equations and including the full global sensitivity matrix saves computational time over the property lagging method and tridiagonal formulation, respectively. The improved efficiency and accuracy of the method may not significantly benefit the analyst for one-dimensional problems, but when the algorithm is extended to multiple dimensions, the advantages could be worth the added development effort. The problems presented in this work are generally "well behaved," and as a result the proposed method would be even more advantageous for longer simulations and highly nonlinear problems.

Acknowledgments

Sandia is a multiprogram laboratory operated by Sandia Corporation, a Lockheed Martin Company, for the United States Department of Energy's National Nuclear Security Administration under Contract DE-AC04-94AL85000. The authors would like to thank Sandia National Laboratories staff members, Dave Kuntz and Don Potter, for their involvement in technical discussions. In addition, A. J. Amar would like to thank Basil Hassan, his manager at Sandia National Laboratories, for the support throughout the project.

References

[1] Moyer, C. B., and Rindal, R. A., "An Analysis of the Coupled Chemically Reacting Boundary Layer and Charring Ablator, Part 2: Finite Difference Solution for the In-Depth Response of Charring Materials Considering Surface Chemical and Energy Balances," NASA CR-1061, June 1968.

[2] Suzuki, T., Sawada, K., Yamada, T., and Inatani, Y., "Thermal Response of Ablative Test Piece in Arc-Heated Wind Tunnel," AIAA Paper 2004-341, Jan. 2004.

[3] Blackwell, B. F., "Numerical Prediction of One-Dimensional Ablation Using a Finite Control Volume Procedure with Exponential Differencing," *Numerical Heat Transfer*, Vol. 14, No. 1, 1988, pp. 17–34. doi:10.1080/10407788808913631

[4] Blackwell, B. F., and Hogan, R. E., "One-Dimensional Ablation Using Landau Transformation and Finite Control Volume Procedure," *Journal of Thermophysics and Heat Transfer*, Vol. 8, No. 2, 1994, pp. 282–287.

[5] Hogan, R. E., Blackwell, B. F., and Cochran, R. J., "Application of Moving Grid Control Volume Finite Element Method to Ablation Problems," *Journal of Thermophysics and Heat Transfer*, Vol. 10, No. 2, 1996, pp. 312–319.

[6] Suzuki, T., Sawada, K., Yamada, T., and Inatani, Y., "Experimental and Numerical Study of Pyrolysis Gas Pressure in Ablating Test Piece," *Journal of Thermophysics and Heat Transfer*, Vol. 19, No. 3, 2005, pp. 266–272.

[7] Chen, Y.-K., and Milos, F. S., "Ablation and Thermal Response Program for Spacecraft Heatshield Analysis," *Journal of Spacecraft and Rockets*, Vol. 36, No. 3, 1999, pp. 475–583.

[8] Chen, Y.-K., and Milos, F. S., "Two-Dimensional Implicit Thermal Response and Ablation Program for Charring Materials on Hypersonic Space Vehicles," AIAA Paper 2000-0206, Jan. 2000.

[9] Chen, Y.-K., and Milos, F. S., "Three-Dimensional Ablation and Thermal Response Simulation System," AIAA Paper 2005-5064, June 2005.

[10] Amar, A. J., "Modeling of One-Dimensional Ablation with Porous Flow Using Finite Control Volume Procedure," M.S. Thesis, North Carolina State University, Raleigh, NC, 2006.

[11] Landau, H. G., "Heat Conduction in a Melting Solid," *Quarterly of Applied Mathematics*, Vol. 8, No. 1, 1950, pp. 81–94.

[12] Kays, W. M., Crawford, M. E., and Weigand, B., *Convective Heat and Mass Transfer*, 4th ed., McGraw–Hill, New York, 2005.

[13] Marvin, J. G., and Akin, C. M., "Combined Effects of Mass Addition and Nose Bluntness on Boundary-Layer Transition," *AIAA Journal*, Vol. 8, No. 5, 1970, pp. 857–863.

[14] Marvin, J. G., and Pope, R. B., "Laminar Convective Heating and Ablation in the Mars Atmosphere," *AIAA Journal*, Vol. 5, No. 2, 1967, pp. 240–248.

[15] Cohen, C. B., and Reshotko, E., "Similar Solutions for the Compressible Laminar Boundary Layer with Heat Transfer and Pressure Gradient," NACA TN 3325, 1955.

[16] Eckert, E. R. G., and Drake, R. M., Jr., *Analysis of Heat and Mass Transfer*, McGraw–Hill, New York, 1972, pp. 432–433.

[17] Eckert, E. R. G., "Engineering Relations for Skin Friction and Heat Transfer to Surfaces in High Velocity Flows," *Journal of the Aerospace Sciences*, Vol. 22, Aug. 1955, pp. 585–587.

[18] Arpaci, V. S., *Conduction Heat Transfer*, Addison–Wesley, Reading, MA, 1966, pp. 129–132.

[19] Gerald, C. F., and Wheatley, P. O., *Applied Numerical Analysis*, 5th ed., Addison–Wesley, Reading, MA, 1994, pp. 72–73.

[20] Blottner, F. G., "Variable Grid Scheme Applied to Turbulent Boundary Layers," *Computer Methods in Applied Mechanics and Engineering*, Vol. 4, Sept. 1974, pp. 179–194. doi:10.1016/0045-7825(74)90033-4

[21] Blottner, F. G., "Variable Grid Scheme for Discontinuous Grid Spacing and Derivatives," *Computers and Fluids*, Vol. 8, Dec. 1980, pp. 421–434. doi:10.1016/0045-7930(80)90004-3

[22] Roache, P. J., *Verification and Validation in Computational Science and Engineering*, Hermosa Publishers, Albuquerque, NM, 1998, pp. 114–136.